Laser streaking of dissociating D_2^+ in a strong midinfrared laser pulse

Liang Xu[1] and Feng He[1,2,*]

[1]*Key Laboratory for Laser Plasmas (Ministry of Education) and School of Physics and Astronomy, Collaborative Innovation Center of IFSA (CICIFSA), Shanghai Jiao Tong University, Shanghai 200240, China*

[2]*CAS Center for Excellence in Ultra-intense Laser Science, Shanghai 201800, China*

(Received 25 January 2021; revised 11 May 2021; accepted 26 May 2021; published 14 June 2021)

Laser streaking of photoelectrons has been a well-established technique to extract ultrafast information. In analogy to the streaking of photoelectrons, in this paper, we study the laser streaking of nuclei by numerically simulating the time-dependent Schrödinger equations of D_2^+ in strong laser fields. We first demonstrate the nuclear streaking, where the dissociating wave packet excited by an isolated attosecond pulse and propagating on molecular potential surfaces is streaked by a strong midinfrared laser pulse. Subsequently, we use an attosecond pulse train composing two successive attosecond pulses to initiate the dissociation of D_2^+. Depending on the time delay between the attosecond pulse train and the midinfrared laser pulse, the streaked nuclear wave packets show a novel delay-dependent interference pattern. By tracing the wave-packet evolution in the adiabatic presentation, the complicated dissociation pathways are revealed. Based on the streaked nuclear pattern, one may conceive a strategy to probe the real-time nuclear streaking process and extract instantaneous dynamics information experimentally.

DOI: 10.1103/PhysRevA.103.063108

I. INTRODUCTION

Rapid advances of laser technologies provide a broad stage for the studying of ultrafast physics [1,2]. Benefiting from the generation of ultrashort attosecond pulses [3–5], many ultrafast processes have been investigated with unprecedented time resolutions [6–10]. Most recently, the birth time delay of zeptoseconds in the photoionization of H_2 has been revealed inconceivably, and thus boosted our understanding into a new area [11].

Exposing a target into the laser field consisting of an attosecond pulse and an infrared laser pulse, the photoelectron initiated by the attosecond pulse may be streaked by the remaining infrared laser pulse. According to conservation of canonical momentum, the ultimate photoelectron momentum $p(t_f)$ is the addition of its initial momentum $p(t_i)$ and $-A(t_i)$ if no other interactions (e.g., the Coulomb attraction) are involved. Here t_i denotes the ionization instant. By scanning the time delay between the attosecond pulse and the infrared pulse, the streaked spectrogram can be obtained. Based on such a principle, the laser streaking camera is developed [12]. Such streaking cameras have been used to explore many fascinating ultrafast scenarios, such as imaging the ultrashort light waves directly [13], measuring the unprecedented attosecond pulse duration [14], and probing the Wigner time delay [8,15]. Using a circularly polarized laser pulse to steer the photoelectron emitted along different angles at distinct times, the angular streaking technique, i.e., attoclock, is invented [16] and has achieved great success. The angular streaking camera works as a stopwatch with attosecond time resolution, and has been used to characterize the carrier envelope phase of an isolated attosecond pulse [17], explore the controversial tunneling time [18–22], the nonadiabatic tunneling [23–26], and multielectron correlated effects [27,28], and even uncover the interplay between nonadiabatic and nondipole effects [29].

Compared with electronic streaking, nuclear streaking is rarely discussed. The main reason is due to the very huge mass of the nucleus. For example, for typical laser parameters used in experiments, such as the wavelength of 800 nm and the intensity of 10^{13} W/cm^2 scale, the maximum laser vector potential is less than 1.0 a.u.. However, the typical D_2^+ nuclear momentum is about 35.0 a.u. in its dissociation process. Hence, the laser field can hardly modulate the nuclear momentum effectively. Alternatively, the nuclear wave packet experiences fast laser oscillations instead of adiabatic electric fields since the timescale of the nuclear propagation on molecular potential surfaces is much longer than the optical period, and thus it is better to use the concept of photons instead of the quasistatic electric field to explain the energy transfer between molecules and lasers. However, for a midinfrared (MIR) or even far-infrared laser pulse, its optical period is comparable to the nuclear movement timescale, hence the deformation of the molecular potential surfaces can severely modify the nuclear kinetic energy. Xu *et al.* studied the dissociation of D_2^+ in a terahertz light pulse, and found that the nuclear ultimate momentum is modulated [30]. More recently, using suchlike laser fields, the electron-localization-resolved rotation is observed during the D_2^+ dissociation [31]. Currently, there are still some problems about the nuclear streaking to be answered. For example, does laser streaking of the nuclear wave packet really exist? How does the nuclear streaking effect modulate the nuclear interference pattern since the dissociative wave packets always propagate on the instantaneous

*fhe@sjtu.edu.cn

potential energy surfaces? Is it possible to view the nuclear streaking in real time?

In this paper, we focus on the nuclear streaking in the dissociation of D_2^+. We first demonstrate the laser streaking of a nuclear wave packet, where an isolated attosecond pulse is used to to trigger the D_2^+ dissociation along the $2p\sigma_u$ state and a time-delay MIR pulse is introduced to steer the dissociating nuclear wave packet. Then we replace the attosecond pulse by an attosecond pulse train composing two successive attosecond pulses in order to see the modulation of the interference pattern in streaking. Depending on the time delay between the attosecond pulse train and the MIR pulse, the interference pattern by the two attosecond pulses in the train may disappear or be reserved. Finally, in order to observe the nuclear streaking in real time, we conceive the following strategy. Firstly, an isolated attosecond pulse triggers the dissociation, then a MIR pulse modifies the potential surfaces, and finally another time-delayed attosecond pulse is used to ionize the dissociating D_2^+. The laser dressed molecular potential information can be extracted by analyzing the ionization fragments.

II. NUMERICAL METHODS

A. Two-level model

In many cases, the dissociation of D_2^+ is governed by the dynamics between the two lowest electronic states, i.e., $1s\sigma_g$ and $2p\sigma_u$. Due to the significantly different masses of nucleus and electron, the Born-Oppenheimer approximation is widely used in the study of molecular dissociation. Hence, the molecular wave packet can be written as

$$\psi(\vec{r}, \mathbf{R}; t) = \chi_g(\mathbf{R}, t)\varphi_g(\vec{r}, \mathbf{R}) + \chi_u(\mathbf{R}, t)\varphi_u(\vec{r}, \mathbf{R}), \quad (1)$$

where $\vec{r}$ and $\mathbf{R}$ are the electron displacement and the internuclear distance vector, respectively. $\varphi_{g/u}(\vec{r}, \mathbf{R})$ denote the orthogonal $1s\sigma_g$ and $2p\sigma_u$ electronic states. The corresponding nuclear rovibrational states $\chi_{g/u}(\mathbf{R}, t)$ are governed by the two-level time-dependent Schrödinger equation (Hartree atomic units are used throughout unless stated otherwise)

$$i\frac{\partial}{\partial t}\begin{pmatrix}\chi_g(\mathbf{R}, t)\\ \chi_u(\mathbf{R}, t)\end{pmatrix} = (H_0 + H_I)\begin{pmatrix}\chi_g(\mathbf{R}, t)\\ \chi_u(\mathbf{R}, t)\end{pmatrix}, \quad (2)$$

where the field-free Hamiltonian H_0 is defined as

$$H_0 = \begin{pmatrix}\frac{\mathbf{P}_R^2}{2M} + V_g(\mathbf{R}) & 0\\ 0 & \frac{\mathbf{P}_R^2}{2M} + V_u(\mathbf{R})\end{pmatrix}. \quad (3)$$

$M = 1836$ a.u. is the reduced nuclear mass of D_2^+, and $\mathbf{P}_R$ is the nuclear momentum operator. $V_{g/u}(\mathbf{R})$ denote the potential surfaces for the $1s\sigma_g$ and $2p\sigma_u$ states, respectively [32], as shown in Fig. 1(b). The interaction Hamiltonian in the length gauge and electric dipole approximation is written as

$$H_I = \begin{pmatrix}0 & \mathbf{D}(\mathbf{R})\cdot\mathbf{E}(t)\\ \mathbf{D}(\mathbf{R})\cdot\mathbf{E}(t) & 0\end{pmatrix}, \quad (4)$$

where $\mathbf{D}(\mathbf{R})$ is the $\mathbf{R}$-dependent transition dipole moment between the two electronic states [33]. $\mathbf{E}(t)$ is the laser electric field vector.

We solve Eq. (2) by using the Crank-Nicholson technique with the time step $\delta t = 0.2$ a.u. [34]. The two-dimensional spatial range of simulation is $[-70, 70]$ a.u. $\times$ $[-70, 70]$ a.u.

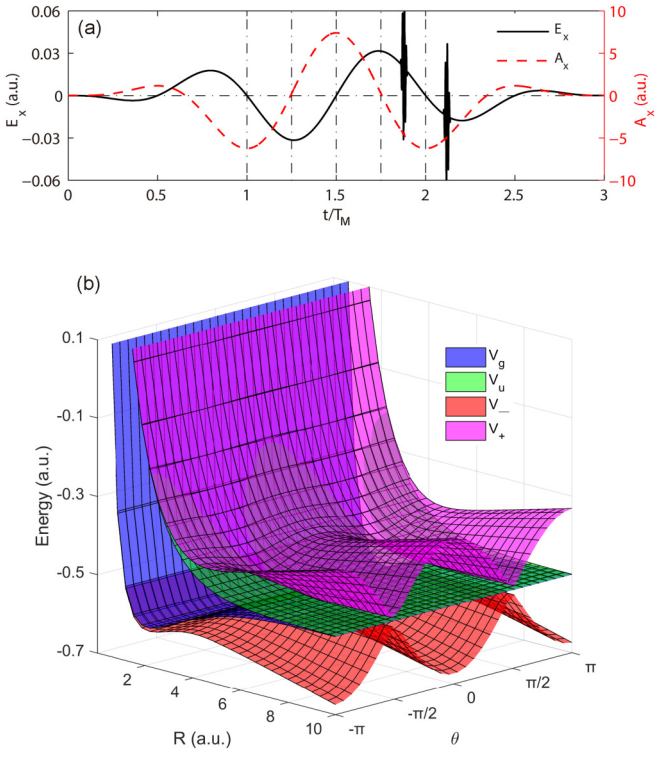

FIG. 1. (a) The laser configuration with an attosecond pulse train and a MIR pulse. The two attosecond pulses in the train have laser parameters: $\lambda_{1/2} = 106$ nm, $I_{1/2} = 1.0 \times 10^{14}$ W/cm^2, four periods, a sin^2 envelope, $\Delta t_a = 8.01$ fs, and $\Delta t_b = 0.5T_M$. The MIR laser with $\lambda_M = 10$ μm has a peak intensity $I_M = 4.0 \times 10^{13}$ W/cm^2. (b) The two-dimensional potential energy surfaces for D_2^+. $V_g(\mathbf{R})$ (blue) and $V_u(\mathbf{R})$ (green) represent the field-free potential surfaces, respectively. The x axis linearly polarized MIR field induces the anisotropy molecular potential surfaces, $V_-(\mathbf{R})$ (red) and $V_+(\mathbf{R})$ (magenta). The instantaneous intensity of MIR pulse is 4.0×10^{13} W/cm^2.

with 7000 points in each dimension. The simulation box is big enough to keep the entire dissociation signal and thus no absorbing boundaries are needed. Initially, $\chi_g(\mathbf{R}, t_0)$ is the ground rovibrational state of D_2^+, and $\chi_u(\mathbf{R}, t_0)$ is empty. We obtain the initial state by using the imaginary time propagation method [35]. Molecular nuclear momentum wave functions $\widetilde{\chi}_g(\mathbf{P}_R)$ and $\widetilde{\chi}_u(\mathbf{P}_R)$ are calculated by the Fourier transform of the final wave functions $\chi_g(\mathbf{R}, t_f)$ and $\chi_u(\mathbf{R}, t_f)$ excluding the bound states, respectively. The nuclear momentum distribution after the interaction is $|\widetilde{\chi}_{g+u}(\mathbf{P}_R)|^2 = |\widetilde{\chi}_g(\mathbf{P}_R)|^2 + |\widetilde{\chi}_u(\mathbf{P}_R)|^2$, from which the angle-resolved kinetic energy release (KER) distribution is calculated by

$$P_{\text{all}}(\theta, \text{KER}) = |\widetilde{\chi}_{g+u}(\mathbf{P}_R)|^2 M/|\mathbf{P}_R|. \quad (5)$$

In this model, we confine $\mathbf{R}$ in a two-dimensional (x, y) plane, and the emission angle θ is defined as $\tan\theta = \mathbf{P}_{Ry}/\mathbf{P}_{Rx}$. Such a two-dimensional calculation is acceptable since no dynamics occurs in the third dimension except for the wave-packet free expansion.

B. Beyond the two-level model

Since the electron dynamics is restricted in the two lowest electronic states, the above two-level dissociation model

cannot include the molecular ionization. To make sure that the ionization is negligible in the nuclear streaking study, and to view the nuclear streaking in real time, we build the following model:

$$i\frac{\partial}{\partial t}\Phi_\theta(R,z;t) = [H_0 + V_I(t)]\Phi_\theta(R,z;t). \tag{6}$$

Here θ denotes the molecular orientation. The field-free Hamiltonian H_0 is

$$H_0 = -\frac{1}{2M}\frac{\partial^2}{\partial R^2} - \frac{1}{2\mu_e}\frac{\partial^2}{\partial z^2} + V_0(R,z), \tag{7}$$

and V_0 is the Coulomb potential [36,37]

$$V_0(R,z) = \frac{1}{R} - \frac{1}{\sqrt{(z+R/2)^2 + \left(\frac{\beta(R)}{5}\right)^2} + \frac{1}{\beta(R)} - \frac{\beta(R)}{5}} - \frac{1}{\sqrt{(z-R/2)^2 + \left(\frac{\beta(R)}{5}\right)^2} + \frac{1}{\beta(R)} - \frac{\beta(R)}{5}}. \tag{8}$$

Here, $R = |\mathbf{R}|$ is the internuclear distance, and z is the electron position along the molecular axis. $\mu_e = M/(M+1)$ is the reduced mass of the electron and $\beta(R)$ is the R-dependent soft-core parameter. By properly choosing $\beta(R)$, the potential in Eq. (8) can reproduce the D_2^+ ground-state energy -0.6 a.u. and equilibrium internuclear distance $R_0 = 2.0$ a.u. [36]. Under the electric dipole approximation, $V_I(t)$ describes the laser-molecule interaction in the length gauge

$$V_I(t) = E(t) z\cos\theta, \tag{9}$$

where $E(t)$ is the laser electric field along the x-axis direction. The calculation steps for Eq. (6) are $\delta t = 0.1$ a.u., $\delta R = 0.02$ a.u., and $\delta z = 0.1$ a.u.. R and x span the spatial range [0, 70] a.u. and [−1500, 1500] a.u., respectively. To suppress the unphysical reflection from boundaries, a $\cos^{1/8}$ masking function has been adopted to absorb the undesired ionization signal induced by the MIR pulse [38], though the ionization is to be found negligible. The numerical algorithms used in this model are the same as those used in the two-level model. The numerical convergences for this model and the first model have been checked by using finer spatial and time steps, and almost identical results have been obtained.

III. RESULTS AND DISCUSSIONS

A. The laser streaking of the nuclear wave packets

In this subsection, we use an isolated attosecond pulse or an attosecond pulse train composing two successive attosecond pulses to initiate dissociation, followed by the streaking of a MIR laser pulse. All simulation results in this section are calculated by using the two-level model. The laser electric field is expressed generally as

$$\mathbf{E}(t) = [E_{1,\mathrm{as}}(t) + E_{2,\mathrm{as}}(t) + E_{\mathrm{MIR}}(t)]\mathbf{e_x} \tag{10}$$

with

$$E_{1,\mathrm{as}} = E_1 \sin^2[\pi(t-t_1)/\tau_1]\sin[\omega_1(t-t_1)], \quad t_1 < t < t_1 + 4T_1, \quad t_1 = -0.5\Delta t_a + \Delta t_b + 1.5T_M - 2T_1; \tag{11}$$

$$E_{2,\mathrm{as}} = E_2 \sin^2[\pi(t-t_2)/\tau_2]\sin[\omega_2(t-t_2)], \quad t_2 < t < t_2 + 4T_2, \quad t_2 = 0.5\Delta t_a + \Delta t_b + 1.5T_M - 2T_2; \tag{12}$$

and

$$E_{\mathrm{MIR}} = E_M \sin^2(\pi t/\tau_M)\sin(\omega_M t + \pi), \quad 0 < t < 3T_M. \tag{13}$$

The origin time ($t_0 = 0$ a.u.) is defined as the starting instant of the MIR pulse. t_1 and t_2 denote the starting moments of the first and second attosecond pulses, respectively. Except for their relative delay Δt_a, the two attosecond pulses have the same laser parameters: $\lambda_{1/2} = 106$ nm ($\omega_{1/2} = 0.43$ a.u.), $I_{1/2} = 1.0\times10^{14}$ W/cm^2 ($E_{1/2} = 0.0534$ a.u.), and a duration $\tau_{1/2}$ of four optical periods. Please note that in this paper, the intensities of all attosecond pulses are not stern and much weaker intensities (as weak as 10^9 W/cm^2 in experiments) will give the same conclusion. The attosecond pulse may resonantly excite D_2^+ from the $1s\sigma_g$ state to the $2p\sigma_u$ state. During the dissociation process, a three-cycle MIR laser pulse ($\tau_M = 3T_M$) with the wavelength $\lambda_M = 10$ μm ($\omega_M = 4.56\times10^{-3}$ a.u. and $T_M = 34$ fs) is introduced to streak the nuclear wave packet. Its peak intensity is $I_M = 4.0\times10^{13}$ W/cm^2 ($E_M = 0.034$ a.u.). The time delay between the attosecond pulse train and the MIR pulse is defined as Δt_b. $\Delta t_b < 0$ ($\Delta t_b > 0$) means that the attosecond pulse precedes (lags behind) the MIR pulse. Δt_a and Δt_b are variable in our simulations. In Fig. 1(a), the laser fields are shown when $\Delta t_a = 8.01$ fs and $\Delta t_b = 0.5T_M$. Here all laser fields are polarized along the x axis. Note that if an isolated attosecond pulse is used instead of an attosecond pulse train, the corresponding laser parameters are $\lambda_1 = 106$ nm ($\omega_1 = 0.43$ a.u.), $I_1 = 1.0\times10^{14}$ W/cm^2 ($E_1 = 0.0534$ a.u.), $I_2 = 0$ W/cm^2, and $\Delta t_a = 0$ a.u.

In Fig. 2, we use the laser combination of an isolated attosecond pulse and a MIR pulse and obtain the nuclear momentum distributions (top row) and angle-resolved energy distributions (bottom row). Since the attosecond pulse is linearly polarized along the x axis, no dissociative nuclear signal appears at $\theta = \pm\pi/2$. In panels (a) and (b), the black dashed circle is formulated by $|\mathbf{P}_R| = \sqrt{2M[V_u(R_0) + 0.5]}$, which corresponds to the nuclear momentum acquired without the MIR field. Similarly, the black dashed lines in panels (c) and (d) denote the estimated kinetic energy without the MIR field. As shown in panel (a) with $\Delta t_b = -0.5T_M$, the momentum distribution almost entirely locates inside the circle, which means that the whole nuclear wave packet is decelerated finally. However, when $\Delta t_b = -0.22T_M$, as shown in panel (b), the momentum distribution has two main parts, which are accelerated and decelerated, respectively.

To explain the distinct momentum and KER distributions, we now turn to an adiabatic presentation. In the adiabatic presentation, the molecular potentials are expressed as

$$V_\pm(\mathbf{R},t) = \frac{V_g(\mathbf{R}) + V_u(\mathbf{R})}{2} \pm \sqrt{\frac{[V_g(\mathbf{R}) - V_u(\mathbf{R})]^2}{4} + [\mathbf{D}(\mathbf{R})\cdot\mathbf{E}(t)]^2}, \tag{14}$$

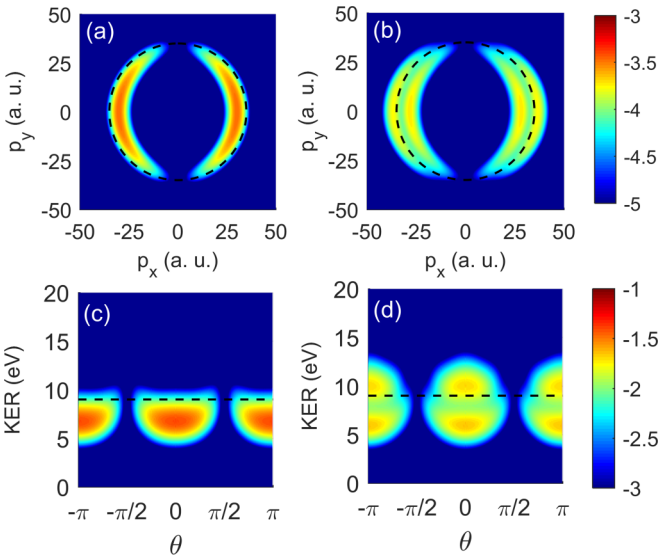

FIG. 2. The two-dimensional momentum distributions (top row) and the corresponding angle-dependent KER spectra (bottom row) induced by a single attosecond pulse and the MIR pulse. (a) and (c) $\Delta t_b = -0.5T_M$. (b) and (d) $\Delta t_b = -0.22T_M$. The intensities of attosecond ($\lambda_1 = 106$ nm) and MIR ($\lambda_M = 10$ μm) pulses are $I_1 = 1.0 \times 10^{14}$ W/cm^2 and $I_M = 4.0 \times 10^{13}$ W/cm^2, respectively. The black dashed lines in every subgraph denote the classical momentum and kinetic energy of the nuclear wave packet when the MIR field is not introduced.

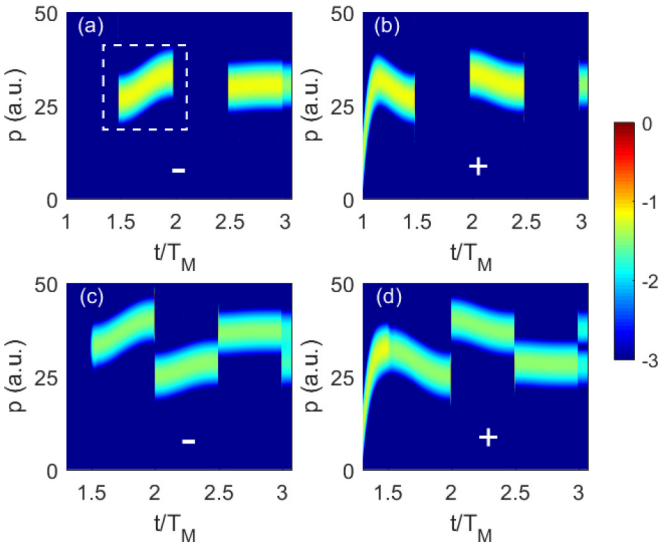

FIG. 3. The time-dependent nuclear momentum distribution $|\widetilde{\chi}_{\pm}(P_R, t)|^2$ along $\theta = 0$ direction on the potential surface $V_{\pm}(\mathbf{R}, t)$. (a) and (b) $\Delta t_b = -0.5T_M$. (c) and (d) $\Delta t_b = -0.22T_M$. The other laser parameters are the same as those used in Fig. 2. The region specified by the white dashed square in panel (a) is to be viewed in real time in Sec. III B.

and the two corresponding orthogonal adiabatic states are

$$\chi_-(\mathbf{R}, t) = \cos(\alpha)\chi_g(\mathbf{R}, t) + \sin(\alpha)\chi_u(\mathbf{R}, t) \quad (15)$$

and

$$\chi_+(\mathbf{R}, t) = -\sin(\alpha)\chi_g(\mathbf{R}, t) + \cos(\alpha)\chi_u(\mathbf{R}, t). \quad (16)$$

Here α satisfies

$$\tan(2\alpha) = -2[\mathbf{D}(\mathbf{R}) \cdot \mathbf{E}(t)]/[V_u(\mathbf{R}) - V_g(\mathbf{R})]. \quad (17)$$

When the internuclear distance is larger than 10 a.u., $V_g(R)$ and $V_u(R)$ are almost degenerate. Therefore, α tends to swap between $\pm\pi/4$ when $E_{\mathrm{MIR}}(t)$ changes directions. The swap of α determines the swap of $\chi_{\pm}(\mathbf{R}, t)$ synchronously. The Fourier transformation of $\chi_{\pm}(\mathbf{R}, t)$ at $R > 10$ a.u. gives the momentum wave packet $\widetilde{\chi}_{\pm}(\mathbf{p_R}, t)$, respectively. $V_{\pm}(\mathbf{R}, t)$ are presented in Fig. 1(b) when the instantaneous electric field is $E_{\mathrm{MIR}}(t) = 0.034$ a.u. [i.e., $I_{\mathrm{MIR}}(t) = 4.0 \times 10^{13}$ W/cm^2].

Here we focus on the dissociative fragments emitted along the x axis since they have the largest momentum change with respect to the case without the MIR pulse. Figure 3 gives the time-dependent nuclear momentum distributions $|\widetilde{\chi}_{\pm}(P_R, t)|^2$ along $\theta = 0$ direction on the potential surface $V_{\pm}(\mathbf{R}, t)$. For the case of $\Delta t_b = -0.5T_M$, as one can see in Figs. 3(a) and 3(b), the dissociative wave packet $\chi_u(\mathbf{R})$ triggered by the attosecond pulse first accelerates on $V_+(\mathbf{R}, t)$ at small nuclear distance where $V_+(\mathbf{R}, t) \approx V_u(\mathbf{R}, t)$. When the wave packet approaches the region around $R = 10$ a.u., the large instantaneous laser electric field uplifts $V_+(\mathbf{R}, t)$ and suppresses $V_-(\mathbf{R}, t)$ adiabatically. Meanwhile, $\chi_u(\mathbf{R})$ changes into $\chi_+(\mathbf{R})$. Then, the dissociative wave packet $\chi_+(\mathbf{R})$ is slowed down on $V_+(\mathbf{R}, t)$. Once the laser field changes the direction, $\chi_+(\mathbf{R}, t)$ and $\chi_-(\mathbf{R}, t)$ swap with each other. However, for $\Delta t_b = -0.22T_M$, as shown in Figs. 3(c) and 3(d), when the wave packet propagates to $R \approx 10$ a.u., the temporary laser field almost vanishes and $\chi_+(\mathbf{R}) \approx \chi_u(\mathbf{R})$ and $\chi_-(\mathbf{R}) \approx \chi_g(\mathbf{R})$. Subsequently, as the laser field starts to increase, α jumps from 0 to $\pi/4$. According to Eqs. (15)–(17), $\chi_u(\mathbf{R})$ becomes the superposition of $\chi_+(\mathbf{R})$ and $\chi_-(\mathbf{R})$. Hence, the dissociating wave packet splits into two parts with almost the same probability. One part $\chi_+(\mathbf{R})$ is decelerated on $V_+(\mathbf{R}, t)$ and the other part $\chi_-(\mathbf{R})$ is accelerated on $V_-(\mathbf{R}, t)$. They both swap with each other at later moments when $E_{\mathrm{MIR}}(t) = 0$.

After understanding the nuclear streaking well, we now replace the isolated attosecond pulse by an attosecond pulse train including two attosecond pluses to study the nuclear streaking, since experimentally an attosecond pulse train is easier to be generated. In addition, an attosecond pulse train can bring interesting interference phenomena beyond the streaking spectrogram.

In Fig. 4, we show the nuclear momentum distributions (top row) and angle-resolved energy distributions (bottom row) for different delays as indicated in the caption. In panels (a) and (b), the momentum distributions shrink and stretch along the horizontal axis, respectively, as can be viewed by comparing the nuclear momentum distributions with the dashed circle. Such deformations are more distinct in the corresponding KER distributions in panels (e) and (f). Comparing (e) and (f), one may find that the energy distribution in (f) is wider than that in (e). In (a) and (e), clear interference structures are presented, and the interference stripes in (e) are separated by about 0.057 a.u.. Usually, the separation equates to $2\pi/\Delta t_a$. Though (g) and (h) are calculated with the same delay Δt_a, the interference is smeared out in (h), which is to be explained a bit later in a discussion.

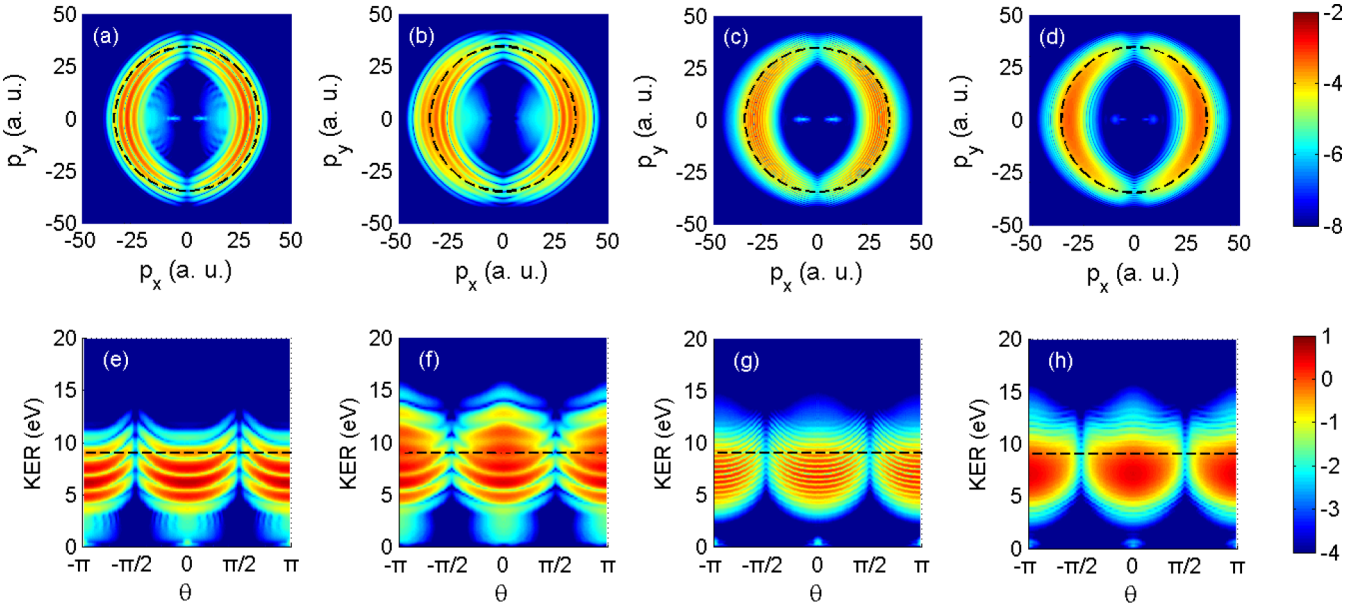

FIG. 4. The two-dimensional momentum distributions (top row) and the corresponding angle-dependent KER spectra (below row) induced by two attosecond pulses and the MIR pulse. (a) and (e) $\Delta t_a = 2.67$ fs, $\Delta t_b = 0$. (b) and (f) $\Delta t_a = 2.67$ fs, $\Delta t_b = 0.3T_M$. (c) and (g) $\Delta t_a = 8.01$ fs, $\Delta t_b = 0$. (d) and (h) $\Delta t_a = 8.01$ fs, $\Delta t_b = 0.25T_M$. The intensities of attosecond ($\lambda_{1/2} = 106$ nm) and MIR ($\lambda_M = 10$ μm) pulses are $I_{1/2} = 1.0 \times 10^{14}$ W/cm^2 and $I_M = 4.0 \times 10^{13}$ W/cm^2, respectively. The black dashed lines are the same as those used in Fig. 2.

To better understand the delay-dependent energy streaking, we pick out the dissociative fragments emitted along $\theta = 0$ and $\pi/3$, and show the Δt_b-dependent KER spectra in Fig. 5.

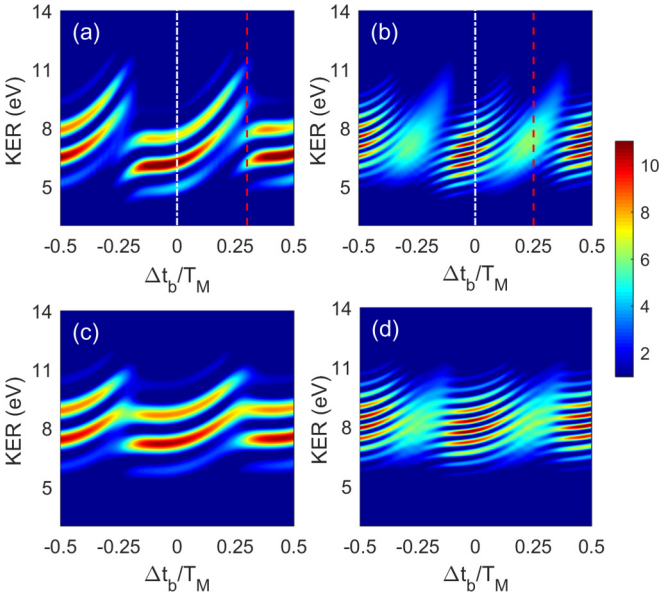

FIG. 5. The KER spectra along the molecular orientation $\theta = 0$ (a) and (b) and $\pi/3$ (c) and (d). (a) $\Delta t_a = 2.67$ fs, $I_M = 4.0 \times 10^{13}$ W/cm^2. (b) $\Delta t_a = 8.01$ fs, $I_M = 4.0 \times 10^{13}$ W/cm^2. (c) $\Delta t_a = 2.67$ fs, $I_M = 1.0 \times 10^{13}$ W/cm^2. (d) $\Delta t_a = 8.01$ fs, $I_M = 1.0 \times 10^{13}$ W/cm^2. The white dot-dashed lines in panels (a) and (b) correspond to the time delays used in (a) and (c) of Fig. 4, respectively. The red dashed lines in panels (a) and (b) mark the time delays used in (b) and (d) in Fig. 4, respectively. The attosecond train has the intensity $I_{1/2} = 1.0 \times 10^{14}$ W/cm^2 and the wavelength $\lambda_{1/2} = 106$ nm.

The four panels correspond to four sets of laser parameters as shown in the caption. Physically, the molecules aligned along different directions experience the effective laser intensity $\propto E^2_{\rm MIR}(t)\cos^2\theta$. Obviously, a laser pulse with a higher effective intensity (4.0×10^{13} W/cm^2 at $\theta = 0$) streaks the nuclei more intensely, and a weaker MIR pulse (1.0×10^{13} W/cm^2 at $\theta = \pi/3$) also produces similar interferometric fringes with different modulation depths, as shown in Figs. 5(c) and 5(d). Most interestingly, in the streaked patterns shown in Figs. 5(b) and 5(d), the interference structures depend on the time delay. For example, at $\Delta t_b = \pm 0.25T_M$, the interference structures almost completely disappear.

We trace the time-resolved momentum distributions along the x axis on the $V_-(\mathbf{R})$ (left column) and $V_+(\mathbf{R})$ (right column) potential surfaces again by using the adiabatic presentation, as shown in Fig. 6. At $\Delta t_a = 2.67$ fs and $\Delta t_b = 0$ in panels (a) and (b) corresponding to the instant marked by the white dot-dashed lines in Fig. 5(a), the nuclear wave packets initiated by the two attosecond pulses, $\chi_1(\mathbf{R})$ and $\chi_2(\mathbf{R})$, both propagate on the $V_+(\mathbf{R})$ adiabatically when they enter the area where $V_g(\mathbf{R})$ and $V_u(\mathbf{R})$ are degenerate. In the later propagation, both $\chi_1(\mathbf{R})$ and $\chi_2(\mathbf{R})$ synchronously swap between $V_-(\mathbf{R})$ and $V_+(\mathbf{R})$ potential surfaces. In other words, $\chi_1(\mathbf{R})$ and $\chi_2(\mathbf{R})$ are always on the same electronic state $V_\pm(\mathbf{R})$ and thus interfere with each other, that is, $|\widetilde{\chi}_{\rm all}(\mathbf{P}_{\rm R}, t)|^2 = |\widetilde{\chi}_{1\pm}(\mathbf{P}_{\rm R}, t) + \widetilde{\chi}_{2\pm}(\mathbf{P}_{\rm R}, t)|^2$. When the time delays are $\Delta t_a = 8.01$ fs and $\Delta t_b = 0.25T_M$ as shown in Figs. 6(e) and 6(f), which corresponds to the instant marked by the red dashed line in Fig. 5(b), the interference disappears. The reason is as follows. The dissociative nuclear wave packet always changes from $\chi_u(\mathbf{R})$ to $\chi_+(\mathbf{R})$ since the potential curve $V_u(\mathbf{R})$ always changes adiabatically into $V_+(\mathbf{R})$ when R increases from 2 to 10 a.u.. Just after $\chi_1(\mathbf{R})$ propagates to the area $R > 10$ a.u., as $\chi_{1u}(\mathbf{R})$ changes into $\chi_{1+}(\mathbf{R})$, the MIR electric field reverses its

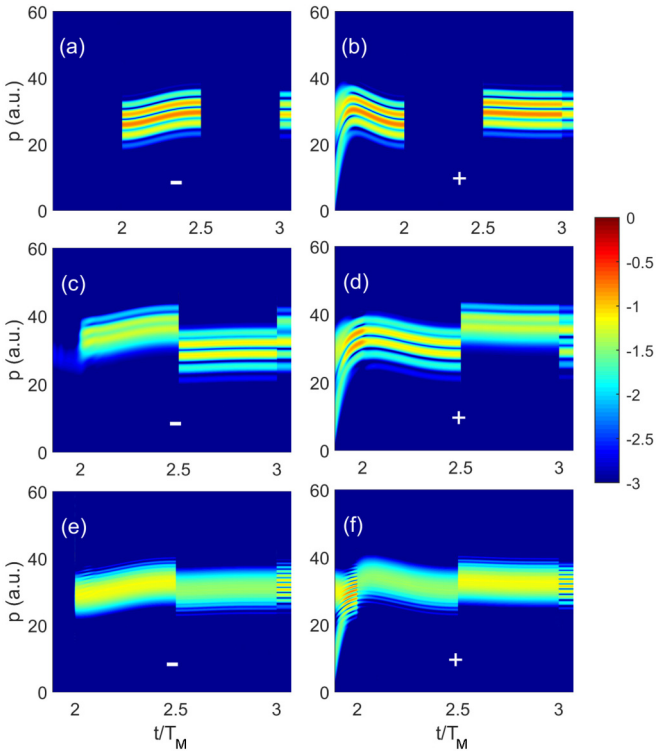

FIG. 6. The time-dependent nuclear momentum distributions along the laser polarization direction ($\theta = 0$). The left column represents $|\widetilde{\chi}_{-}(P_R, t)|^2$ and $|\widetilde{\chi}_{+}(P_R, t)|^2$ in the right one. (a) and (b) $\Delta t_a = 2.67$ fs, $\Delta t_b = 0$. (c) and (d) $\Delta t_a = 2.67$ fs, $\Delta t_b = 0.3T_M$. (e) and (f) $\Delta t_a = 8.01$ fs, $\Delta t_b = 0.25T_M$. The other laser parameters are the same as those used in Fig. 4.

direction, and thus $\chi_{1+}(\mathbf{R})$ swaps into $\chi_{1-}(\mathbf{R})$. However, the latish $\chi_2(\mathbf{R})$ still stays in the area $R < 10$ a.u. when the MIR electric field reverses its direction. When $\chi_2(\mathbf{R})$ enters the area $R > 10$ a.u., it changes into $\chi_{2+}(\mathbf{R})$. Therefore, $\chi_{1-}(\mathbf{R})$ and $\chi_{2+}(\mathbf{R})$ do not propagate on the same potential surface. Since $\chi_{\pm}(\mathbf{R})$ are orthogonal to each other, the interference between $\chi_1(\mathbf{R})$ and $\chi_2(\mathbf{R})$ vanishes, namely, $|\widetilde{\chi}_{\rm all}(\mathbf{P}_{\rm R}, t)|^2 = |\widetilde{\chi}_{1\mp}(\mathbf{P}_{\rm R}, t)|^2 + |\widetilde{\chi}_{2\pm}(\mathbf{P}_{\rm R}, t)|^2$. For $\Delta t_a = 2.67$ fs and $\Delta t_b = 0.3T_M$ in Figs. 6(c) and 6(d) corresponding to the delay indicated by the red dashed line in Fig. 5(a), when the dissociating $\chi_{1u}(\mathbf{R})$ approaches the $R \approx 10$ a.u. region, the MIR electric field happens to be zero, and thus $\chi_{1u}(\mathbf{R})$ is in the superimposition between $\chi_{1-}(\mathbf{R})$ and $\chi_{1+}(\mathbf{R})$ with the same proportion. In the following propagation, the coexistence of $\chi_{1-}(\mathbf{R})$ and $\chi_{1+}(\mathbf{R})$ results in the ultimately wide momentum spectra. However, $\chi_2(\mathbf{R})$ fully changes into $\chi_{2+}(\mathbf{R})$ almost when it just enters the area $R > 10$ a.u.. Therefore, only part of $\chi_1(\mathbf{R})$ interferes with $\chi_2(\mathbf{R})$. One may see that there is a striking interferometric fringe in the low-energy region, but the interference pattern in the highly energetic part is relatively vague, as shown in Figs. 4(b) and 4(f).

The above results have shown that the nuclei of a dissociating D_2^+ can be streaked by a MIR laser pulse and the interference structures imprinted on the dissociating wave packets can be modulated by varying the time delay Δt_a and Δt_b. In the next section, we conceive a strategy to view the nuclear streaking in real time.

B. View the nuclear streaking in real time

According to the analysis in the previous section, the nuclear streaking is associated with the dissociation dynamics on $V_{\pm}(\mathbf{R}, t)$. To resolve the instantaneous dissociation pathways, we may watch the nuclear streaking in real time. Inversely, such real-time watching may further support the picture of nuclear streaking in strong laser fields.

To real-time watch the nuclear streaking, first we use an isolated attosecond pulse to trigger the dissociation of D_2^+. At a certain delay, another isolated attosecond pulse is introduced to ionize the dissociating D_2^+ streaked by the MIR field. Hence, the laser electric field is written as

$$\mathbf{E}(t) = [E_{1,\rm as}(t) + E_{\rm MIR}(t) + E_{2,\rm as}(t)]\mathbf{e}_{\mathbf{x}}, \tag{18}$$

where the expressions for $E_{1,\rm as}(t)$, $E_{\rm MIR}(t)$, and $E_{2,\rm as}(t)$ are the same as Eqs. (11), (13), and (12), respectively. But the laser parameters are different from those used in the previous section. In this calculation, we introduce the first isolated attosecond pulse at $t_1 = 1.0T_M$. This attosecond pulse has the intensity $I_1 = 1.0 \times 10^{14}$ W/cm^2, the wavelength $\lambda_1 = 106$ nm, and a duration of $4T_1$. Then the dissociation process is streaked by a three-cycle MIR field with $\lambda_M = 10$ μm and $I_M = 4.0 \times 10^{13}$ W/cm^2. The first attosecond pulse and the MIR pulse play the same roles as those in the first part about the nuclear streaking in the previous section.

If the second attosecond pulse is tentatively switched off, the time-dependent dissociative nuclear momentum distributions $\widetilde{\chi}_{\pm}(\mathbf{P}_{\rm R}, t)$ on $V_{\pm}(\mathbf{R}, t)$ are shown in the adiabatic presentation in Figs. 3(a) and 3(b), which is calculated by the two-level model. It is obvious that the dissociating wave packet swaps between $\chi_{\pm}(\mathbf{R}, t)$ during the dissociation when the MIR field changes directions. Within the time interval $t = 1.5T_M$ and $2.0T_M$, the nuclear wave packet is completely on $V_{-}(\mathbf{R}, t)$, as marked by the dashed square in Fig. 3(a). During this time interval, we introduce the second attosecond probing pulse at t_2 with $\lambda_2 = 85$ nm ($\omega_2 = 0.54$ a.u.) and $I_2 = 2.0 \times 10^{14}$ W/cm^2 ($E_2 = 0.076$ a.u.) to ionize the dissociating D_2^+. The following results are calculated by using the second model. For ionized D_2^+ fragments, the ultimate nuclear momentum can be approximated as $\mathbf{P}_R(t_f) \approx \mathbf{P}_R(t_2)$. The part contributed by the Coulomb repulsion $\sqrt{2M/R(t_2)}$ is small since $R(t_2)$ is larger than 15 a.u. for laser parameters we used. Please note that though the nucleus is still streaked directly by the MIR laser field after the ionization of D_2^+, the two nuclei are streaked synchronously and thus their relative momentum is not affected during the subsequent streaking process. By scanning t_2 from $1.5T_M$ to $2.0T_M$, the real-time nuclear momentum distribution $\mathbf{P}_R(t_2)$ can be reproduced, as shown in Fig. 7(a). The nuclear wave packet indeed accelerates and its velocity increases monotonically from 25 to 35 a.u., which all agree with those predicted in Fig. 3(a). Such an agreement also verifies our adiabatic explanation for the dissociation of D_2^+ in long-wavelength laser fields.

The instantaneous acceleration of the nuclear wave packet on $V_{-}(\mathbf{R}, t)$ can be obtained via $\mathbf{a}(t_2) = d\overline{\mathbf{P}}_R(t_2)/(Mdt_2)$. Here $\overline{\mathbf{P}}_R(t_2)$ denotes the expected value of the nuclear momentum distribution at $t = t_2$. Physically, for the adiabatic dissociation in the MIR laser field, such acceleration corresponds to $\mathbf{a}(t_2) = -\partial V_{-}(\mathbf{R}, t_2)/(M\partial R)$. Please note that the

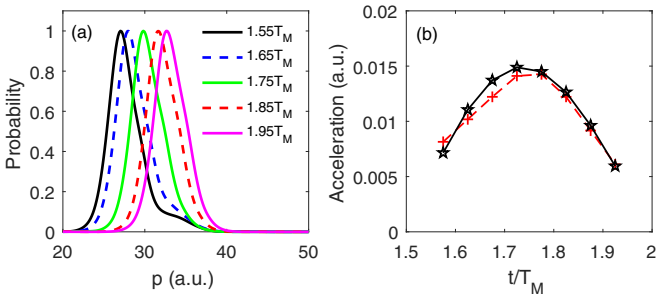

FIG. 7. (a) The extracted nuclear momentum distributions normalized by their own maximum values for the $\theta = 0$ oriented molecule. The laser parameters of the first attosecond and MIR laser pulses are the same as those used in Figs. 3(a) and 3(b). The second probing attosecond pulse $\lambda_2 = 85$ nm with the intensity $I_2 = 2.0 \times 10^{14}$ W/cm^2 is applied at variable t_2, as shown by the legend in (a). (b) The instantaneous acceleration of the nuclear wave packet. The black solid line is calculated by $\mathbf{a}(t_2) = -\partial V_-(R, t_2)/(M\partial R)$ according to Eq. (14). The red dashed line is obtained by $\mathbf{a}(t_2) = d\overline{\mathbf{P}}_R(t_2)/(Mdt_2)$.

laser-dressed potential curves $V_\pm(\mathbf{R}, t)$ almost depend linearly on the internuclear distance $\mathbf{R}$ at the area $R > 10$ a.u., and its slope is only sensitive to the instantaneous laser intensity but not to R. The accelerations obtained in these two ways are comparable, as shown in Fig. 7(b). Furthermore, from the time-dependent acceleration, one may reconstruct the time-resolved potential curves.

IV. CONCLUSIONS

To summarize, we have studied the dissociation of D_2^+ in a MIR laser field. Different from the dissociation in lasers with the wavelength 800 nm, it is more convenient to investigate the dissociation in the quasistatic presentation, in which the electronic eigenstates correspond to the well localization in one of the nuclei. A typical scenario in such a MIR field is laser streaking of the nuclear wave packet. To demonstrate the laser streaking, we first used an attosecond pulse to initiate the dissociation, and the following propagation in the MIR-dressed potentials contributes to the streaked pattern. Then, by using an attosecond train, we found the interference between the two nuclear wave packets may be modulated. The real-time streaking of nuclei can be obtained by introducing another time-delayed attosecond pulse to ionize the MIR-dressed D_2^+. The delay-dependent ionized fragments map the instantaneously dressed potential. Just like the multiphoton and tunneling are the two asymptotic behaviors in ionization, the laser streaking of nuclei is in the opposite side of the well-accepted one-photon, three-photon, or net-two-photon dissociation pathways. Laser streaking of nuclei not only offers a view angle to understand the molecular dissociation in MIR laser pulses, but also modifies the dissociation process. For example, a strong terahertz laser field may severely change the conical intersection of two potentials of D_2^+, and thus change the angular distributions of dissociation fragments. Looking forward, in the dissociation of nucleus (e.g., the deuteron breaks into a proton and a neutron by absorbing a γ photon, $D + \gamma \rightarrow p + n$), the proton may be streaked in the laser field. This process is very similar to the electron streaking in photoionization of atoms. In the dissociation of nuclei, the proton streaking pattern can tell the moment of nuclear breaking. In this sense, the nuclear streaking may work as a zeptosecond- or even yoctosecond-resolved stopwatch.

ACKNOWLEDGMENTS

This work was supported by Innovation Program of Shanghai Municipal Education Commission (2017-01-07-00-02-E00034), National Key R&D Program of China (2018YFA0404802), National Natural Science Foundation of China (NSFC) (Grants No. 11925405 and No. 91850203), and Shanghai Shuguang Project (17SG10). Simulations were performed on the π supercomputer at Shanghai Jiao Tong University.

[1] T. Brabec and F. Krausz, Rev. Mod. Phys. **72**, 545 (2000).
[2] F. Krausz and M. Ivanov, Rev. Mod. Phys. **81**, 163 (2009).
[3] P. M. Paul, E. S. Toma, P. Breger, G. Mullot, F. Augé, Ph. Balcou, H. G. Muller, and P. Agostini, Science **292**, 1689 (2001).
[4] G. Sansone *et al.*, Science **314**, 443 (2006).
[5] M. Hentschel, R. Kienberger, Ch. Spielmann, G. A. Reider, N. Milosevic, T. Brabec, P. Corkum, U. Heinzmann, M. Drescher, and F. Krausz, Nature (London) **414**, 509 (2001).
[6] M. Huppert, I. Jordan, D. Baykusheva, A. von Conta, and H. J. Wörner, Phys. Rev. Lett. **117**, 093001 (2016).
[7] M. Ossiander *et al.*, Nature (London) **561**, 374 (2018).
[8] M. Schultze *et al.*, Science **328**, 1658 (2010).
[9] L. Seiffert *et al.*, Nat. Phys. **13**, 766 (2017).
[10] I. Jordan, M. Huppert, D. Rattenbacher, M. Peper, D. Jelovina, C. Perry, A. V. Conta, A. Schild, and H. J. Wörner, Science **369**, 974 (2020).
[11] S. Grundmann *et al.*, Science **370**, 339 (2020).
[12] R. Kienberger *et al.*, Nature (London) **427**, 817 (2004).
[13] E. Goulielmakis *et al.*, Science **305**, 1267 (2004).
[14] T. Gaumnitz, A. Jain, Y. Pertot, M. Huppert, I. Jordan, F. Ardana-Lamas, and H. J. Wörner, Opt. Express **25**, 27506 (2017).
[15] A. L. Cavalieri *et al.*, Nature (London) **449**, 1029 (2007).
[16] P. Eckle, M. Smolarski, P. Schlup, J. Biegert, A. Staudte, M. Schöffler, H. G. Muller, R. Dörner, and U. Keller, Nat. Phys. **4**, 565 (2008).
[17] P. L. He, C. Ruiz, and F. He, Phys. Rev. Lett. **116**, 203601 (2016).
[18] P. Eckle, A. N. Pfeiffer, C. Cirelli, A. Staudte, R. Dörner, H. G. Muller, M. Büttiker, and U. Keller, Science **322**, 1525 (2008).
[19] H. C. Ni, U. Saalmann, and J. M. Rost, Phys. Rev. Lett. **117**, 023002 (2016).
[20] N. Camus *et al.*, Phys. Rev. Lett. **119**, 023201 (2017).
[21] U. S. Sainadh *et al.*, Nature (London) **568**, 75 (2019).

[22] A. S. Kheifets, J. Phys. B: At. Mol. Opt. Phys. **53**, 072001 (2020).
[23] K. L. Liu, H. C. Ni, K. Renziehausen, J. M. Rost, and I. Barth, Phys. Rev. Lett. **121**, 203201 (2018).
[24] K. L. Liu, S. Q. Luo, M. Li, Y. Li, Y. D. Feng, B. J. Du, Y. M. Zhou, P. X. Lu, and I. Barth, Phys. Rev. Lett. **122**, 053202 (2019).
[25] H. C. Ni, U. Saalmann, and J. M. Rost, Phys. Rev. A **97**, 013426 (2018).
[26] H. C. Ni, N. Eicke, C. Ruiz, J. Cai, F. Oppermann, N. I. Shvetsov-Shilovski, and L. W. Pi, Phys. Rev. A **98**, 013411 (2018).
[27] A. N. Pfeiffer, C. Cirelli, M. Smolarski, D. Dimitrovski, M. Abu-samha, L. B. Madsen, and U. Keller, Nat. Phys. **8**, 76 (2012).
[28] V. P. Majety and A. Scrinzi, J. Mod. Opt. **64**, 1026 (2017).
[29] H. C. Ni *et al.*, Phys. Rev. Lett. **125**, 073202 (2020).
[30] T. Y. Xu and F. He, Phys. Rev. A **88**, 043426 (2013).
[31] L. Xu and F. He, Phys. Rev. A **102**, 023106 (2020).
[32] T. E. Sharp, At. Data. Nucl. Data. Tables **2**, 119 (1970).
[33] D. E. Ramaker and J. M. Peek, At. Data Nucl. Data Tables **5**, 167 (1973).
[34] J. Crank and P. Nicholson, Math. Proc. Cambridge Philos. Soc. **43**, 50 (1947).
[35] R. Kosloff and H. Tal-Ezer, Chem. Phys. Lett. **127**, 223 (1986).
[36] B. Feuerstein and U. Thumm, Phys. Rev. A **67**, 043405 (2003).
[37] L. Xu, C. X. Hu, and F. He, Phys. Rev. A **99**, 033420 (2019).
[38] F. He, C. Ruiz, and A. Becker, Phys. Rev. A **75**, 053407 (2007).